

Tomographic reconstruction of the runaway distribution function in TCV using multispectral synchrotron images

T.A. Wijkamp^{1,2}, A. Perek², J. Decker³, B. Duval³, M. Hoppe⁴, G. Papp⁵, U.A. Sheikh³, I.G.J. Classen², R.J.E. Jaspers¹, the TCV team^a and the EUROfusion MST1 team^b

¹ Department of Applied Physics, Eindhoven University of Technology, Eindhoven 5600 MB, Netherlands

² DIFFER - Dutch Institute for Fundamental Energy Research, De Zaaie 20, 5612 AJ Eindhoven, the Netherlands

³ Ecole Polytechnique Fédérale de Lausanne (EPFL), Swiss Plasma Center (SPC), CH-1015 Lausanne, Switzerland

⁴ Department of Physics, Chalmers University of Technology, SE-41296 Gothenburg, Sweden

⁵ Max Planck Institute for Plasma Physics, D-85748 Garching, Germany

^a See author list S. Coda et al., *Nuclear Fusion*, 59: 112014 (2019) (<https://doi.org/10.1088/1741-4326/ab25cb>)

^b See author list of B. Labit et al. *Nuclear Fusion*, 59: 086020 (2019) (<https://doi.org/10.1088/1741-4326/ab2211>)

Abstract.

Synchrotron radiation observed in a quiescent TCV runaway discharge is studied using filtered camera images targeting three distinct wavelength intervals. Through the tomographic SART procedure the high momentum, high pitch angle part of the spatial and momentum distribution of these relativistic particles is reconstructed. Experimental estimates of the distribution are important for verification and refinement of formation-, decay- and transport-models underlying runaway avoidance and mitigation strategy design. Using a test distribution it is demonstrated that the inversion procedure provides estimates accurate to within a few tens of percent in the region of phase-space contributing most to the synchrotron image. We find that combining images filtered around different parts of the emission spectrum widens the probed part of momentum-space and reduces reconstruction errors. Next, the SART algorithm is used to obtain information on the spatiotemporal runaway momentum distribution in a selected TCV discharge. The momentum distribution is found to relax towards an avalanche-like exponentially decaying profile. Anomalous high pitch angles and a radial profile increasing towards the edge are found for the most strongly emitting particles in the distribution. Pitch angle scattering by toroidal magnetic field ripple is consistent with this picture. An alternative explanation is the presence of high frequency instabilities in combination with the formation of a runaway shell at the edge of the plasma.

1. Introduction

Successful operation of the next generation of tokamaks is threatened by runaway electron (RE) formation during a thermal quench. To deal with the issue disruptions should be avoided, and a disruption mitigation system needs to be in place [1, 2]. Design of the latter relies on numerical models founded on a detailed understanding of the runaway and background plasma behaviour [3]. Experimental verification of theories on both fronts calls for ways to diagnose both (i) conditions in post-disruptive plasmas and (ii) the real and momentum-space distribution of the runaway electrons.

Synchrotron radiation, emitted by runaways gyrating in the tokamak magnetic field [4], is sensitive to details of the RE distribution function. This renders the emission a promising source for passively diagnosing runaways [3]. Pioneering observations in the 90's [5, 6] sparked synchrotron studies in a wide range of tokamaks over the last two decades, a comprehensive overview of which is provided by Tinguely et al [7].

Synchrotron spectra are readily obtained with the use of spectrometers. While this approach has been applied with considerable success [8], it has been demonstrated that multiple distributions can be fit to a single spectrum [9]. In an effort to provide additional constraints to the distribution function, filtered 2D visible imaging has been employed on multiple devices [4, 7, 10–15]. The downside of using camera images is the loss of spectral information. An attempt has been made to circumvent part of this deficiency by splitting the RGB components of an image [10]. This approach however suffers from line radiation pollution, obscuring dimmer parts of the pattern.

In this work a novel method for adding the spectral dimension to 2D camera imaging is presented, relying on recent advances in multispectral imaging systems [16, 17] which are described in section 2. Simultaneous 2D imaging of synchrotron emission in several separated narrow wavelength bands widens the probed region of momentum- and real-space, allowing for tighter constraints on the spatiotemporal evolution of the runaway momentum-distribution. The experimental method is put to the test during TCV runaway discharges, addressed in section 3.

The additional constraints facilitate a tomographic approach to reconstructing the momentum-

and real-space distribution of the runaways from synchrotron images. Linear systems of equations linking the distribution and image are generated through the synthetic diagnostic SOFT [13], as will be addressed in section 4. The reconstruction approach is outlined in section 5, and is the first attempt to obtain a RE distribution function from synchrotron images without imposing constraints on the distribution shape. Using an avalanche-like test distribution the performance of the algorithm is assessed. It is found that the distribution is reconstructed with an accuracy up to a few tens of percent in the part of phase-space contributing most to synchrotron image.

In section 6 the reconstruction approach is applied to TCV experimental data. The momentum-space profile is found to relax towards an exponentially decaying avalanche-like profile. Anomolously high pitch angles and a radial profile increasing with plasma minor radius are found for the well-constrained part of phase-space. Magnetic field ripple and high frequency instabilities are proposed as underlying pitch angle scattering mechanisms. The main conclusions of the paper are revisited in section 7.

2. Multispectral imaging systems in runaway experiments

The advances in synchrotron runaway diagnostics described here are made possible by the recent development of multispectral imaging systems in the context of divertor detachment studies [16, 17]. These imaging devices are capable of recording light from a fusion plasma at several different narrow wavelength intervals using multiple cameras with the same field-of-view. The synchrotron patterns at TCV were gathered using the MultiCam system depicted in figure 1. Light enters the system via the relay optic (i), and is subsequently distributed amongst different channels with the use of beam splitters (ii). All channels consist of a filter (iii), objective (iv) and a camera sensor (v). Hardware and acquisition specifications are identical to that of the optical cavity based multispectral system MANTIS and are described in detail by Perek et al [16]. Used camera settings can be found in the supplementary material.

The cameras are equipped with a 950 nm (full-width-half-maximum 10 nm), 800 nm (10 nm), 640.6 nm (1.7 nm) and a Balmer alpha filter at 656.2 nm (1.1 nm). The former three are placed with the aim of

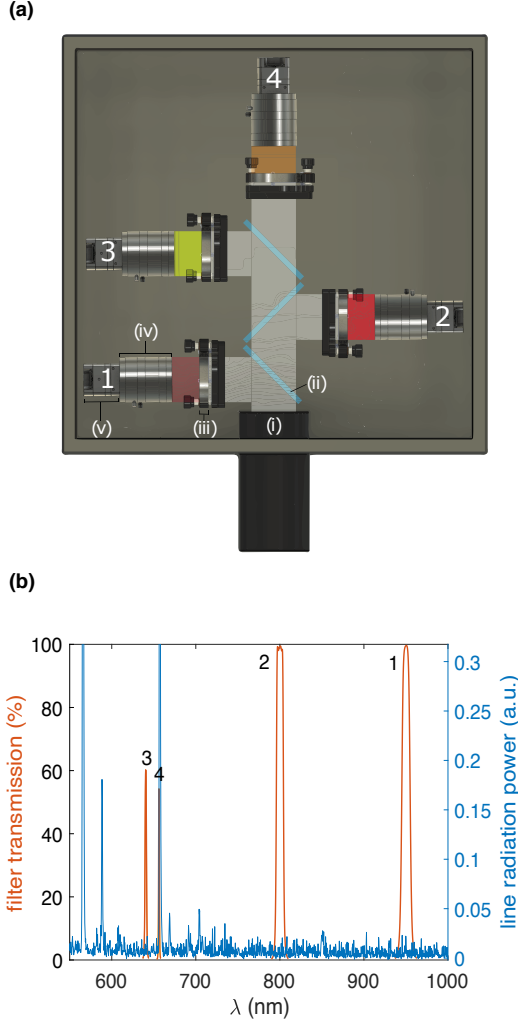


Figure 1. Schematic top view of the optical diagnostic MultiCam (a). Light from a tokamak plasma is relayed to the entrance of the box (i). Using a set of beamsplitters (ii) the light is distributed amongst four different camera channels. Each channel has a distinct narrow band optical interference filter (iii), the transmission curves T of which are shown (b) as a function of wavelength λ . This same plot shows line-radiation recorded by a top-down spectrometer in TCV shot 64717 between 1 and 1.5 s. The transmitted portion of the light is focused on a sensor (v) with the use of an objective (iv).

studying synchrotron radiation. The latter is installed to record emission from the cold edge of the plasma. Synchrotron filter transmission ranges were chosen so as to (i) avoid pollution by line emission, (ii) while maximizing the spectral coverage, (iii) keeping in mind the sensitivity curve of the sensors which tends to zero near the infrared. The line-radiation emission spectrum for a typical quiescent runaway shot is shown in figure 1b, and is obtained by integrating top-down spectrometer data in shot 64717 between 1 and 1.5 s. Note that pollution is low for channels 1-3 as intended. The cameras have the capability of adjusting gain and exposure real time in response to the recorded

signal. This means that low intensity light sources can be studied, whilst avoiding saturation if the intensity increases on a time scale of a few ms or more.

Camera sensors are calibrated with the use of an integrating sphere and a light source with known emission characteristics. Calibrations are performed in full diagnostic configuration with exception of the tokamak optical window, so that optical vignetting losses are accounted for. A signal to photons/s conversion factor is obtained, averaged over the transmission band of the corresponding filter. Calculations show that the inconsistency between the synchrotron spectra and calibration source spectrum for the 10 nm full-width-half-maximum filters leads to relative conversion factor errors which do not exceed 1 percent. Extensive characterizations of readout noise, shot noise and near-saturation non-linear noise has been performed. As a result the signal dependent readout uncertainties are known on a pixel-to-pixel basis.

The position, viewing direction, field-of-view and image distortion of the full optical configuration are obtained after installation of the setup using the EURATOM camera calibration software Calcam [18]. A camera model is fit to a set of matching points in a camera image and detailed TCV CAD model. The outcome is used as input for synthetic diagnostics used in interpreting synchrotron radiation as well as the undistortion of experimentally obtained images. Calibration details are found in the supplementary material.

Positioning of the camera, at central height $z = 0$ m, is in accordance with the counter current runaway movement and synchrotron emission direction. As depicted in figure 2, the camera has a tangential view of the plasma, facing the REs head-on. A typical quiescent-phase TCV synchrotron pattern for a runaway beam at camera height is shown in figure 2b. The undistorted pattern is overlayed on the calibrated view of the TCV CAD model to give an indication of the field-of-view.

3. Synchrotron radiation in TCV quiescent-phase

Validity assessment of the iterative tomographic reconstruction method presented here is aided by the unique geometry of synchrotron patterns observed in TCV. Synthetic reconstruction of their features requires an accurate estimate of the runaway distribution function. Judging whether or not the estimate is consistent with expectations requires knowledge of the experimental scenario, which is described in this section.

The synchrotron radiation patterns addressed here appear in the quiescent-phase of a subset of circular plasma TCV runaway discharges. Here,

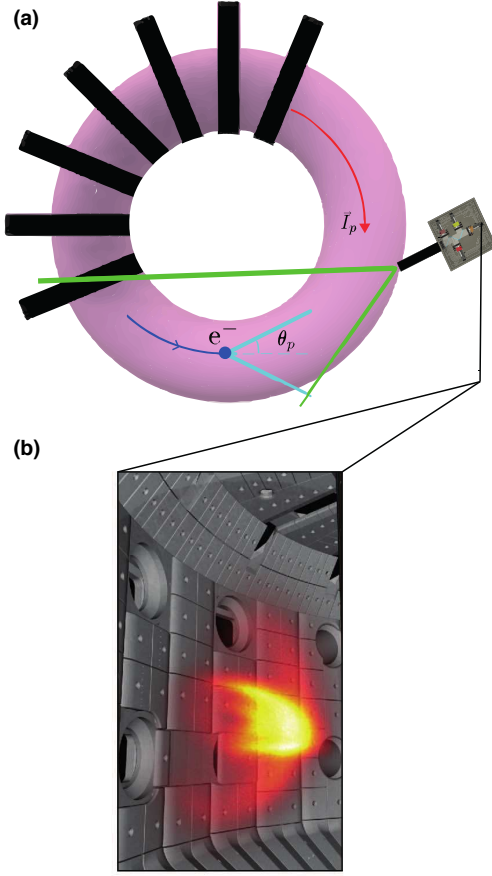


Figure 2. MultiCam configuration in the TCV tokamak (a). The MultiCam viewing cone is indicated (green) along with the plasma current I_p (red) which opposes the runaway movement (blue). The runaways emit radiation along their velocity vector. In a guiding-center picture the relativistic particles follow the magnetic field and emit radiation in a hollow cone along their guiding-center. The half opening angle is equal to the runaway pitch angle θ_p . A typical synchrotron image in TCV is shown (b), overlaid on the calibrated MultiCam view of the TCV CAD model.

shot 64717 is highlighted, whose plasma parameter evolution is shown in figure 3. Peak plasma density and temperature evolution (a) are based on a radial coordinate mapping of Thomson scattering data [19]. By sustaining a sufficiently low electron density and an electric field of 0.2-0.3 V/m, estimated from the temporally smoothed applied loop voltage, the Connor-Hastie critical field [20] is surpassed (d). Runaway production is evidenced by the hard X-ray signal (e) from the scintillator based PhotoMultiplier Tube for hard X-rays (PMTX), and X-ray noise on the MultiCam images. This bremsstrahlung originates from runaway-wall collisions. As opposed to a gas injection triggered disruption scenario, only a small part of the current is carried by relativistic electrons. Note that the sudden increase in PMTX signal at 0.65 s

corresponds to the point in time when the vertical plasma position (b) stabilizes, and comes with a 10 kA jump in the plasma current (c).

In a subset of shots characterized by a relatively high loop voltage light appears on the channels 1-3 as shown in figure 4. Since (i) the source appears to be continuous, (ii) spectrometers not viewing the runaways head-on do not record the emission and (iii) no line radiation is expected to show up on the first three channels, it can be concluded that it is in fact synchrotron radiation which is observed by MultiCam. This conclusion is reinforced by SOFT simulations, which show patterns highly representative of the experimental results [14]. The integrated synchrotron signals shown in figure 3f rise until 1.2 s after which the intensity stabilizes, indicating a balance in the mechanism populating the visible region of phase-space with runaway energy and particle losses.

TCV shot 64717 is of a quiescent nature, the low density flat top not being perturbed throughout the shot. Such a state, with limited runaway current fraction, lends itself for characterization of the background plasma with the available diagnostics. For the purpose of assessing the plausibility of the obtained runaway distribution in the light of the plasma parameter evolution, the quiescent scenario is therefore the preferred one. All synchrotron images shown in this work were taken at 1.357 s in the stable pattern phase. Median filtering is applied to remove X-ray white noise.

4. Synthetic synchrotron diagnostic SOFT

Before demonstrating a novel reconstruction approach to extract energy, pitch angle and spatial information on the runaways from synchrotron images, the synthetic synchrotron diagnostic SOFT [13] is briefly introduced. This tool bridges the gap between experimentally observed patterns and the runaway distribution function. The code constructs a Green function G , also called response function, from a magnetic field geometry and detector details using guiding-center theory. This response function links an arbitrary distribution function f_e in flux surface coordinate ρ , momentum p and pitch angle θ_p to a power distribution P_{synch} over the specified detector. In this work momentum is normalized to the product of electron mass m_e and the speed of light c . In calculating $G(\rho, p, \theta_p)$ SOFT takes into account the (p, θ_p) dependence of the emission spectrum. Also it incorporates the highly non-isotropic nature of synchrotron emission, which is emitted along the velocity vector of the runaway. Therefore only light from REs moving parallel to the detector line-of-sight can be observed. The theory underlying the code rests

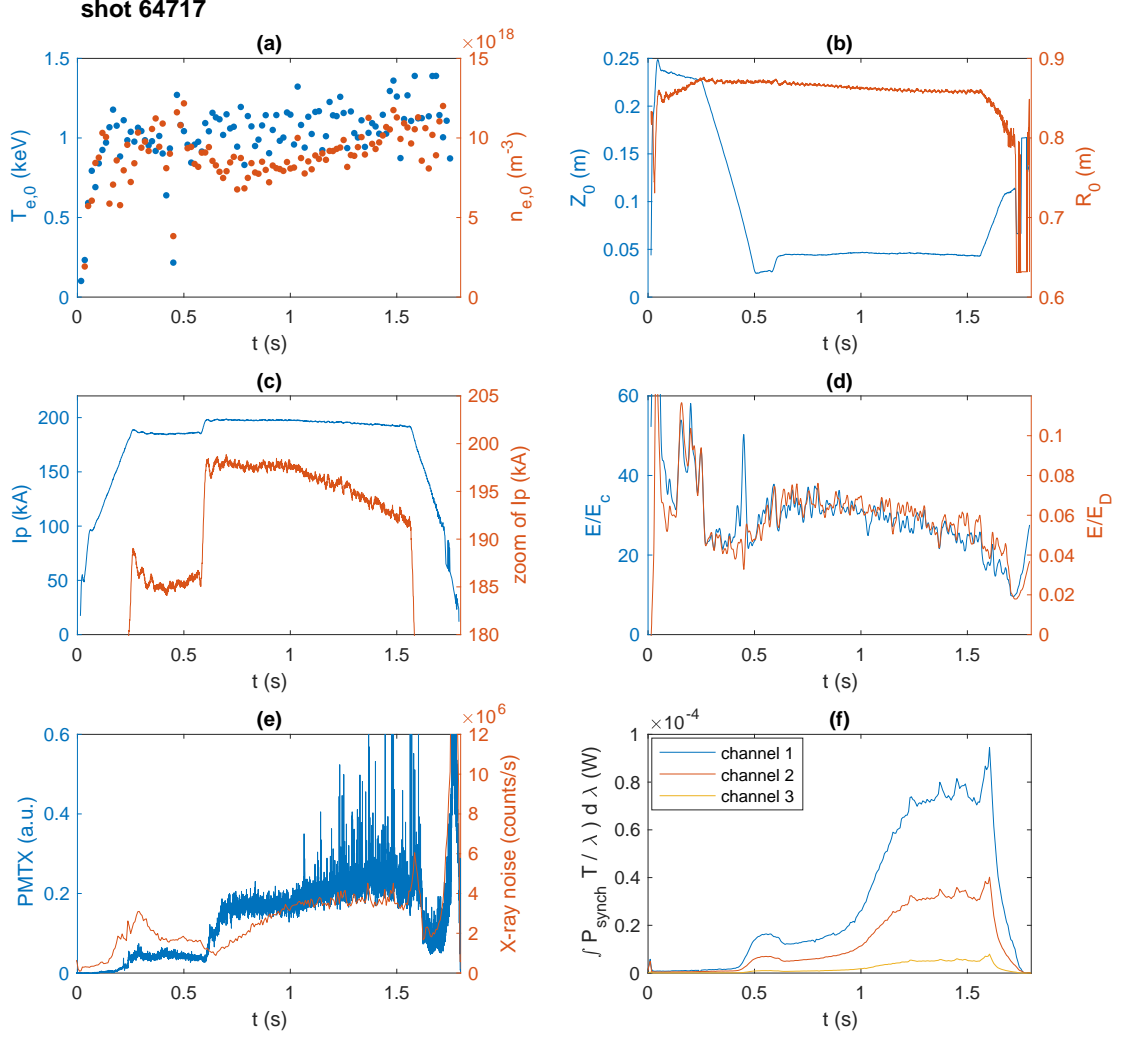


Figure 3. Plasma parameter and diagnostic signal evolution during TCV shot 64717. Thomson scattering data provides an estimate for electron temperature and density (a). The plasma density is sufficiently low for the on-axis electric field to exceed the Connor Hastie critical field (d), setting the conditions for runaway production. Significant RE formation is expected on the basis of the ratio of electric field to Dreicer field shown in the same plot. Runaway production is evidenced by a hard X-ray signal (e) from the PMTX and X-ray noise on MultCam, as well as a rise over time in total recorded intensity on the synchrotron dedicated MultiCam channels (f). During the course of the shot the plasma is translated vertically downwards (b) until 0.65s, after which a jump in plasma current (c) and PMTX signal is observed.

on the assumptions of toroidal symmetry of f_e and the poloidal runaway transit time being much smaller than the runaway collision time. The relation between the power load on pixel i and the RE distribution is:

$$P_{\text{synch},i} = \int \int \int \int G_i(\rho, p, \theta_p, \lambda) f_e(\rho, p, \theta_p) p^2 \sin(\theta_p) T(\lambda) d\rho dp d\theta_p d\lambda. \quad (1)$$

Here the response function has been weighed by the transmission curve $T(\lambda)$ of the camera filter, and the phase-space Jacobian $J = p^2 \sin(\theta_p)$. The required magnetic field geometry is obtained from TCV's

Grad-Shafranov solver LIUQE [21], and the camera location, viewing direction and distortion follow from the Calcam calibration.

Note that at high energies the runaways can experience a significant drift orbit shift, shifting the synchrotron pattern towards the outboard side of the tokamak [22]. This behaviour is corrected for to first order in SOFT, as described in recent work by Hoppe et al [15].

Synchrotron radiation patterns are often dominated by the contribution from a narrow part of runaway phase-space. It is the location where the product

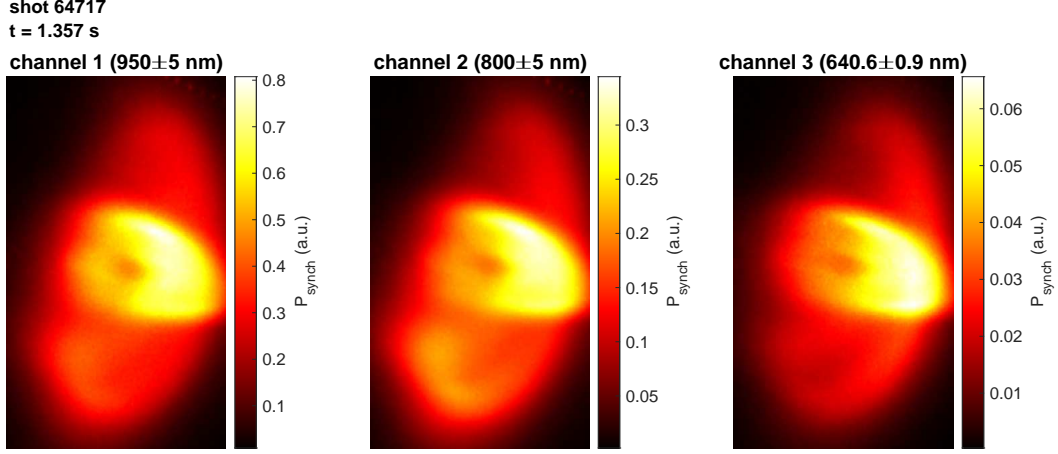


Figure 4. Synchrotron radiation patterns observed in TCV at 1.357 s into shot 64717. The filters of channels 1,2 and 3 have central wavelengths at 950, 800 and 640.6 nm respectively.

GJf_e peaks that contributes most to what a camera observes, and this quantity is therefore referred to in this work as the contribution function. After reconstructing a distribution function f_e from an experimental pattern, GJf_e plays an important role in the interpretation of the found f_e . Changes in f_e only affect the fitting accuracy where the contribution function is significant, so that only in this part of phase-space the reconstruction is expected to be an accurate indication of the real distribution. What contribution qualifies as significantly high will be addressed in the next section.

5. Tomographic reconstruction of the RE distribution from SOFT response functions

Backwards modelling of the runaway population from synchrotron images has to this date relied on analytical or numerical multi-parameter models for the momentum-space distribution [15]. This approach effectively tackles the mathematical difficulty of having to estimate the population of all points in 3D phase-space, which amount to a great number of free parameters. Using the constraints imposed by all pixel values for the multispectral images, an attempt is made in this work to let go of the analytical solution and perform a free reconstruction of the runaway distribution. The motivation for retaining this high level of flexibility are unsuccessful first attempts at explaining the TCV synchrotron patterns using kinetic theory [14]. It is therefore not along the line of expectations that the actual distribution will follow a known analytical solution.

5.1. Tomographic reconstruction method

This section will outline the tomographic approach which is adopted for estimating the solution to the

system of equations linking the distribution to the image via the response function:

$$P_{\text{synch},i} = \sum_j (GJ)_{ij} f_{e,j}, \quad (2)$$

where $(GJ)_{ij}$ is the transmission corrected product of the response function and Jacobian for pixel i and phase-space index j , the latter referring to a specific point in (ρ, p, θ_p) space. The equations for the pixels in all available image channels together form a linear system of equations, for which the distribution solution is approximated using the simultaneous algebraic reconstruction technique (SART) [23, 24]. SART is an iterative way of converging towards a solution minimizing the difference between the synthetic image GJf_e and the real image P_{synch} , using the difference between the two to update all points in the distribution simultaneously:

$$f_{e,j}^{l+1} = f_{e,j}^l + \Delta f_{e,j}^l|_{\text{SART}} + \Delta f_{e,j}^l|_{\beta_m} + \Delta f_{e,j}^l|_{\beta_\rho}. \quad (3)$$

The distribution increment in each step l first of all depends on the SART contribution itself:

$$\Delta f_{e,j}^l|_{\text{SART}} = \frac{\lambda_r}{\sum_i (GJ)_{ij}} \cdot \sum_i \frac{(GJ)_{ij}}{\sum_j (GJ)_{ij}} \left(P_{\text{synch},i} - (GJ)_{ij} f_{e,j}^l \right)$$

The pre-factor to the sum is the relaxation parameter which governs the speeds of convergence, and is modified through the parameter λ_r . The SART modification is based on the difference between all synthetic and experimental pixel values, the term between brackets, weighed by the response function for the given pixel and distribution element. The distribution increments $\Delta f_{e,j}^l|_{\beta_m}$ and $\Delta f_{e,j}^l|_{\beta_\rho}$ impose a certain smoothness on the solution in momentum- and

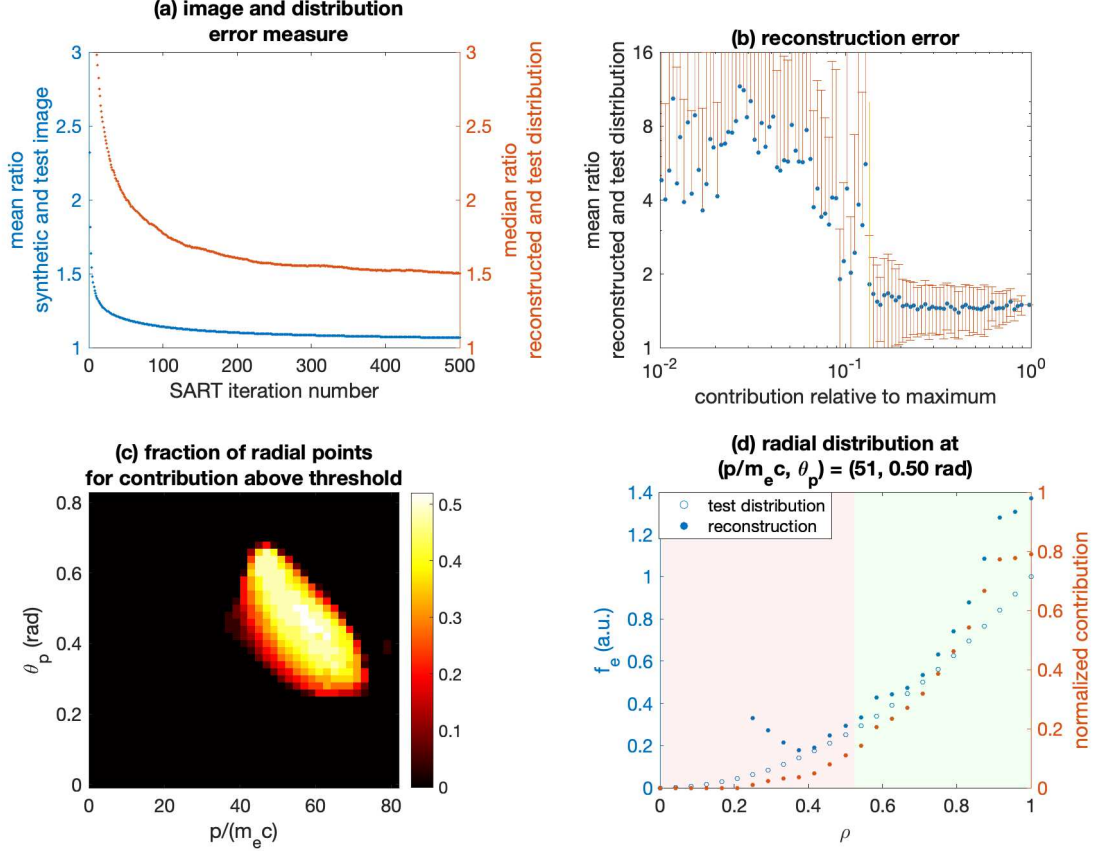


Figure 5. Accuracy assessment of the SART reconstruction approach for an avalanche-like distribution function. No smoothing is applied in the 500 SART iterations used for the reconstruction. a) Evolution of the mean image and median distribution error. For the image comparison, only pixels with an intensity larger than 1 percent of the maximum intensity are examined. Distribution points with a contribution function GJf_e value larger than 10 percent of the maximum are considered. b) Ratio between the reconstructed and input distribution as a function of contribution of the reconstructed distribution to the total image. The definition of the ratio is such that the largest of the two is divided by the smallest, so that 1 indicates perfect resemblance. c) momentum-space map of the fraction of flux surface points above the normalized contribution threshold of 0.135. The threshold is based on the data in figure (b). d) For a normalized momentum $p/m_e c$ of 51, and a pitch angle of 0.50 rad, the test distribution and its reconstruction are depicted as a function of normalized minor radius. The right axis shows the normalized contribution function GJf_e . The red shaded region indicates where the contribution drops below 0.135, and the reconstruction is expected to be less accurate than a factor of 2. Note that below $\rho \sim 0.4$ the contribution is negligible, and large deviations between the reconstructed and real distribution start to become apparent.

real-space respectively. This is achieved by invoking a penalty based on the population difference between a point in phase-space and its neighbours:

$$\Delta f_{e,j}^l|_{\beta_m} = -\beta_m \left(N_{n,m} f_{e,j}^l - \sum_{n=1}^{N_{n,m}} f_{e,n}^l \right),$$

$$\Delta f_{e,j}^l|_{\beta_\rho} = -\beta_\rho \left(N_{n,\rho} f_{e,j}^l - \sum_{n=1}^{N_{n,\rho}} f_{e,n}^l \right).$$

Here $N_{n,m}$ is the number of neighbours on the (p, θ_p) grid, and $N_{n,\rho}$ the number of neighbours in the radial direction. The index n refers to the distribution index of these adjacent elements of f_e . Note that the imposed

smoothness is controlled separately for momentum- and real-space through the parameters β_m and β_ρ .

The SART algorithm is terminated after a predefined number of steps, or when the relative change in the total distribution;

$$\sum_{p, \theta_p} |f_{e[p, \theta_p]}^l - f_{e[p, \theta_p]}^{l-1}| / \sum_{p, \theta_p} f_{e[p, \theta_p]}^{l-1}, \quad (4)$$

reaches a specified threshold. The influence of the smoothness operators on the solution accuracy and convergence speed is assessed later in this section.

5.2. Accuracy assessment of the SART method

To assess how the accuracy and convergence speed of the SART algorithm depend on the solver parameters λ_r , β_m and β_ρ , a test distribution is constructed. An analytical avalanche distribution of the form [25]:

$$f_e = \frac{C_0(\rho)}{\cos(\theta_p)p} \exp \{C_1(\rho) \cos(\theta_p)p\} \exp \{C_2(\rho) \tan(\theta_p) \sin(\theta_p)p\}, \quad (5)$$

is used, where the coefficients $C_{0,1,2}$ all depend on the flux surface coordinate. From the SOFT response functions for TCV shot 64717 at 1.357 s, the camera images for channels 1 through 3 are generated. These images are then perturbed using a pixel intensity dependent noise level, and fed to the SART algorithm. This allows one to compare the reconstructed distribution with the actual one for distributions of various complexities.

For all simulations performed in this work the response functions are generated on a 41×42 momentum, pitch angle grid ranging from $(p/m_e c, \theta_p) = (1, 0 \text{ rad})$ to $(81, 0.82 \text{ rad})$. The original flux surface resolution is 100 to ensure smooth synthetic patterns, but binned into 25 points to reduce memory demands. For the same reason experimental images are binned 8 by 8 to reduce the response function size.

5.2.1. Smooth radially dependent profile

To approach an experimentally realistic distribution, a flux surface dependent momentum-space profile is used. This is achieved through a ρ dependent value of the avalanche coefficients. $C_{0,1,2}$ are tuned so as to generate a synchrotron pattern resembling those in figure 4. C_2 is left at a constant -0.3 , while C_1 decreases linearly from -0.08 to -0.14 between the center and edge of the plasma. C_0 is chosen in a way that assures that $f_e = \rho^2$ at a normalized momentum of 51, and pitch angle of 0.50 rad . Intensity dependent noise is added by scaling all intensities between 0 and 4096, matching the camera sensor signal levels, and then taking the square root of each pixel as its standard deviation. From each pixel value distribution an arbitrary integer is drawn.

For a relaxation parameter of $\lambda_r = 0.95$ the evolution of the mean ratio between synthetic and real pixels as a function of SART iterations is depicted in figure 5a. In computing the mean, only pixels with an intensity above a fraction of 0.01 of the image maximum have been considered. The pixel ratio R_i has been defined such that the largest value, synthetic or real, is divided by the smallest one:

$$R_i = \max \left[\frac{P_{\text{synch},i-\text{synthetic}}}{P_{\text{synch},i-\text{real}}}, \frac{P_{\text{synch},i-\text{real}}}{P_{\text{synch},i-\text{synthetic}}} \right]. \quad (6)$$

Perfect correspondence of the reconstructed image therefore corresponds to a value of 1. This error measure weighs an underestimation by a factor of 2 the same as an overestimation by a factor of 2. Similarly, the figure also depicts the median distribution ratio evolution for phase-space elements which have a contribution value GJf_e above 10 percent of the peak value. The contribution function is here based on the original distribution.

The image error is a strictly decreasing function of the number of iterations. After 500 iterations, taking roughly 5 minutes on an Intel i9 core, the relative error is reduced to 6.6 percent. The main quantity of interest is however the distribution function error. As shown, the distribution error follows the decreasing trend. After the indicated number of iterations the median of the relative errors is 50 percent. This error should be put in the context of the f_e spread in the considered region of phase-space which spans 4 orders of magnitude. The stark decrease in f_e with momentum and pitch angle is captured well by the reconstruction method.

An important question to ask is what part of the reconstructed distribution is to be trusted. In figure 5b the distribution ratio error and its standard deviation, are plotted against the normalized contribution of each phase-space element to the image. Normalization is with respect to the element of f_e contributing most to the perceived intensity. A clear drop in the error is observed above a GJf_e value of 0.135. The location of the corresponding points is visualized in figure 5c. Reconstructions are clearly only to be trusted there where the distribution has a significant contribution to the image. The synthetic image is not sensitive to features elsewhere in the distribution and the synchrotron footage can therefore not be used to constrain all of momentum- and real-space.

The contribution is not just a function of momentum, but also of flux surface coordinate. It is the edge of the distribution which dominates the synthetic image, and large deviations between the real and reconstructed distribution are found near the core of the plasma. To illustrate this, the distribution is plotted as a function of ρ for the momentum-space point $(p/m_e c, \theta_p) = (51, 0.50 \text{ rad})$ in figure 5d. The reconstruction ratio error is below 37 percent for $\rho > 0.4$. Further inwards, the contribution function drops to zero and large deviations from the real distribution are observed.

What level of GJf_e is sufficient for a reconstruction from experimental images to be trusted remains undetermined. The accuracy assessment does indicate that the SART algorithm can locally obtain results accurate to within a factor of 2, spanning over a considerable fraction of phase-space. Equally important, the

analysis points towards a prominent role of the contribution function in interpretation of a reconstructed distribution. Lastly, figure 5 reveals a clear trade-off between accuracy and speed. Time dependent reconstructions covering several tens of frames are however well within reach, despite little time having been devoted to speed optimization of the analysis framework.

5.2.2. Influence of smoothing parameters

The influence of tuning the smoothness parameters is evaluated using the same distribution function. For values of β_m below 0.01, the solution for normalized GJf_e above 0.1 is affected by less than ± 10 percent. The reconstruction is accurate up to lower values of GJf_e . This is likely due to the pull from the constrained part of the distribution on the unconstrained part. Whether this behaviour is desirable is not evident, as the reverse is true as well; the mean error in the edges of the trusted part is raised by introducing smoothing. As β_m approaches 0.1 the error as a function of iteration number is no longer strictly decreasing and has a local minimum. Performance decreases and the median distribution error increases above a factor of 2. Smoothing ought to be kept below the level of a few percent.

Imposing smoothness in the radial direction yields more promising results. Reconstructions are accurate up to smaller contribution values and the median ratio error of this population drops significantly with respect to the non-smoothed case. A smoothness value of $\beta_\rho = 0.1$ yields a median ratio error, above the 10 percent of maximum contribution threshold, of 1.21 after 500 SART iterations. This is a clear improvement over the 1.50 ratio achieved without smoothing. The algorithm speed is not compromised. This is an upper limit as to what smoothing is advised. Going above the level of 0.1 yields problems similar to those observed for high values of β_m . The artificial smoothing becomes a dominant factor in determining the distribution shape and the error function is no longer strictly decreasing, leading to an elevation of error levels.

5.2.3. Flux surface dependent energy cut-off

The limits of the reconstruction method will be tested using a jump in the distribution. Due to a disturbance propagating inwards from the edge to the $\rho = 0.7$ surface, all runaways with a normalized momentum larger than 30 are lost from this portion of the plasma. The result is a sudden jump in both momentum-space and radial direction.

Performing the SART reconstruction, it is observed that the image convergence is slower than for the earlier distribution as shown in figure 6a. Increasing the number of SART iterations to 5000 it is found that the ratio eventually drops below 1.4, but the dis-

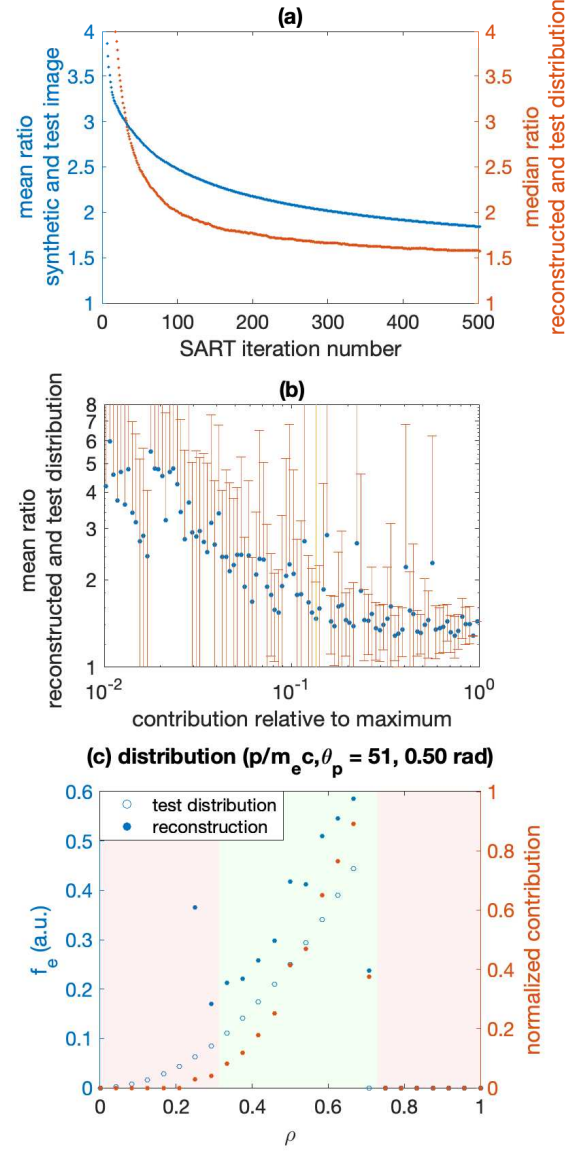


Figure 6. Accuracy assessment for the SART method. The distribution is of an avalanche form, but all runaways with normalized momentum larger than 30 at $\rho > 0.7$ have been removed. a) Evolution of the thresholded mean image and median distribution error. b) Ratio between the reconstructed and input distribution as a function of contribution to the total image. c) Radial distribution at a fixed momentum and pitch angle, showing the reconstructed radial discontinuity. The part of the distribution for which the reconstruction error is expected to be lower than a factor of 2 is indicated in green.

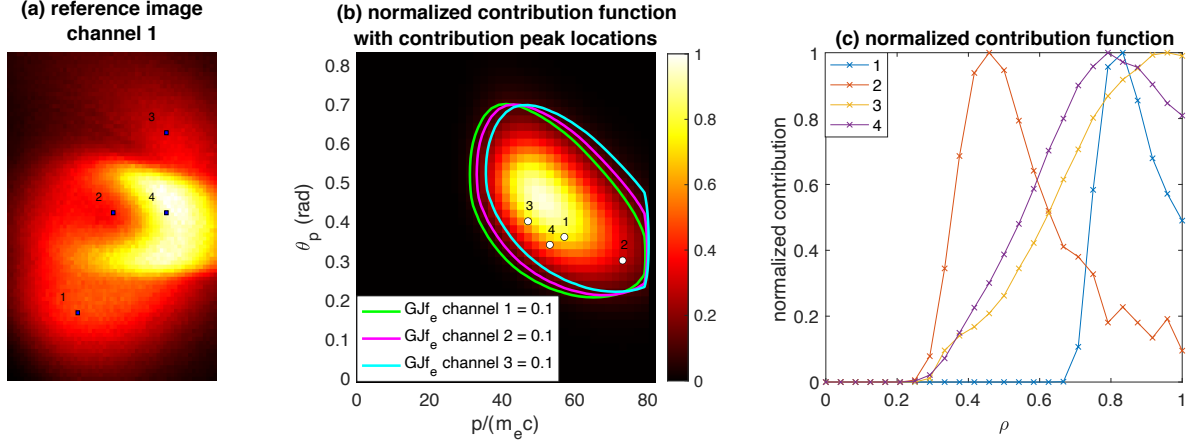


Figure 7. Spectral and spatial dependence of the contribution function for the avalanche-like distribution from section 5.2. a) Binned synchrotron image associated with the distribution. 4 points are labelled, for which the peak in the contribution function is indicated in figure b. b) Normalized contribution function averaged over the three channels. The colored contours indicate the $GJf_e = 0.1$ boundary, and show that the probed region of momentum-space moves towards higher momenta for smaller central filter wavelengths. c) For the 4 points in the image the average flux surface contribution is shown. Different parts of the image contain information on different parts of the spatial distribution.

tribution error changes little from 500 iterations onwards. The ratio error as a function of the contribution function is depicted in figure 6b, and shows the same behaviour as for the more continuous distribution. The SART algorithm appears capable of handling the steep energy barrier. This statement is backed up by the radial profile at $(p/m_e c, \theta_p) = (51, 0.50 \text{ rad})$ shown in figure 6c. At $\rho = 0.7$ a sudden drop in the reconstructed population is observed, matching the location of the barrier in the real distribution. There is a transition region between the occupied and empty part of real-space of a single radial point.

Applying radial smoothing elevates the error, which is to be expected given the discontinuity in the radial profile. This should be taken into account when analyzing experimental data. Consistency of the smoothed and non-smoothed reconstructed distribution should be checked before analyzing the distribution from the smoothed approach.

In conclusion, it has been shown that the unconstrained SART method is able to retrieve the test distribution with a relative accuracy of a few tens of percents for all elements contributing significantly to the synthetic image. To stay below a relative error of a factor of 2, typically only elements with a contribution at a level above 10 percent of the maximum contribution should be considered for the discussed experimental setup.

5.3. Added value of multispectral imaging

As shown, distribution reconstructions are only accurate where the phase-space contribution to the image is sufficiently high. The merit of the distribution

reconstruction method therefore depends on the extent of the phase-space region to which the synchrotron diagnostic is sensitive. Here, the test distribution is used to demonstrate the added value of multispectral synchrotron imaging. It is shown that the spectral- and spatial resolution provide a complementary widening of the probed momentum- and real-space.

To illustrate the point, first consider the contribution function at four different parts of the synchrotron image associated with the test distribution. Figure 7b displays the normalized contribution function for the integrated image, averaged over the three camera channels. On top of this map, the peak locations in the contribution functions for the four separate pixels are shown. Note that different parts of the image predominantly constrain different parts of the runaway phase-space. The flux surface dependence of the contribution functions is portrayed in figure 7c. It shows that positions 1, 3 and 4 mainly receive light from runaways at the edge of the plasma, while position 2 is sensitive to the distribution closer to the core. The peak positions in momentum-space are tied to the radial contribution profiles. Moving from the center of the plasma to the edge, the RE pitch angle required for the camera line-of-sight to be parallel to the runaway velocity vector increases. Therefore, the pixels which probe the edge of the distribution are expected to be more sensitive to higher pitch angles, as is indeed observed in figure 7b.

Next, consider the effect of the central filter wavelength on the probed region of phase-space. The $GJf_e = 0.1$ bounds for the three different channels are indicated in figure 7b. It is found that channels with a shorter central wavelength probe a higher (p, θ_p) region of momentum-space. This is a direct

consequence of the fact that the synchrotron emission peak moves from the infrared towards the visible with increasing momentum and pitch angle. Thus, the contribution from the REs with highest (p, θ_p) to the total image increases with decreasing wavelength. A larger spread in the probed momentum-space can be achieved by increasing the separation in filter central wavelength. For MultiCam and other visible light cameras the significant line emission of hydrogen and regularly encountered impurities below ~ 600 nm limit the possible extend of such an optimization.

Interestingly, extending the range of considered wavelengths broadens the ellipse-like contribution peak region along its minor axis. The sensitivity spread accomplished by adding the spectral dimension to 2D imaging is thus complementary to that achieved by the spatial resolution itself. Multispectral imaging systems essentially act as a large collection of absolutely calibrated spectrometers with coarse wavelength resolution and known spatial orientation, providing sufficient coverage of phase-space to make the SART reconstruction possible.

To quantify the increase in reconstruction performance by having multiple image channels, the image and distribution accuracy for SART input from a single channel are compared to those for input from all three channels. Allowing both reconstructions to last 100 s, the single channels approach yields a smaller mean image ratio error of 1.06, as compared to the 1.11 for the three channels approach. Apparently, with the increased number of equations to satisfy, finding an exact match to the image data is complicated by using multiple channels. The distribution error however shows the reverse trend. Using a single channel yields a mean ratio error of 2.13, while this is only 1.64 for the three channel case. As distribution reconstruction is the sole aim of the SART algorithm, this increase in performance is the leading argument to favour multiple channel reconstruction over the use of a single image.

6. Origin of TCV synchrotron pattern

6.1. Experimental reconstruction results

Using the SART algorithm an attempt is made to estimate the runaway distribution corresponding to the TCV synchrotron images displayed in figure 4. Changes to the image error and the distribution function are marginal after 20 iterations. To allow for fast time sequence reconstructions, the number of iterations is therefore not increased beyond this point. The relaxation parameter λ_r is set at 0.95, and for the present case it is observed that radial smoothing has little influence on the convergence speed and so is turned off. For the SART input, all three camera channels are used. Also for the reconstruction

of f_e from experimental images it is found that the image error is twice as large compared to the single image reconstruction. Based on the results from the test distribution in the previous section, using all channels is however expected to yield a more accurate distribution result, which is the main aim of the analysis presented here.

The reconstruction results at time 1.357 s into TCV shot 64717 are portrayed in figure 8. Figures 8a and 8b show a comparison between the experimental and synthetic image. Both the overall pattern shape and the intensity distribution are comparable, the mean image ratio error above the 1 percent intensity threshold dropping to 1.65 after 20 SART iterations. The corresponding momentum-space distribution integrated over all flux surfaces is shown in figure 8c. The contour lines indicate the contribution function normalized to its maximum value. It shows the region of maximum contribution is at high pitch angle and momentum, with the peak at $(p/m_e c, \theta_p) = (60, 0.53 \text{ rad})$. The momentum-space profile is discussed in more detail in section 6.3

Figure 8d shows the fraction of flux surface points satisfying the criterion $GJf_e/\max(GJf_e) > 0.07$ at each point in momentum-space. This bound was chosen by comparing the total image contribution below some level of GJf_e to the accumulated image uncertainty. The map indicates the region of momentum-space where reconstructions are expected to yield accurate results to within a few tens of percent. Note that for a given energy and pitch angle, the distribution shape is only to be trusted for a sub selection of radial points.

For one of the points in momentum space contributing strongly to the image, namely $(p/m_e c, \theta_p) = (59, 0.52 \text{ rad})$, the radial profile is shown in figure 8e. At high momenta and pitch angles the distribution is an increasing function of ρ . Mechanisms which could lead to such a profile are discussed in section 6.4.

6.2. Reconstruction uncertainty

Besides the systematic errors in the guiding center theory and reconstruction approach, the estimated distribution has an uncertainty associated with (i) uncertainties in the input image and (ii) uncertainties in the camera calibration. Since the reconstruction method does not specify a direct relation between the input image and output distribution, it is not clear cut how the errors propagate to f_e . Here, a Monte Carlo approach is used to quantify the effect of both sources.

As mentioned in section 2, experimental image uncertainties are known on a pixel to pixel basis. This allows one to add random noise to the original image by drawing a value from the distribution function of each individual pixel. Repeating this process N_{image} times

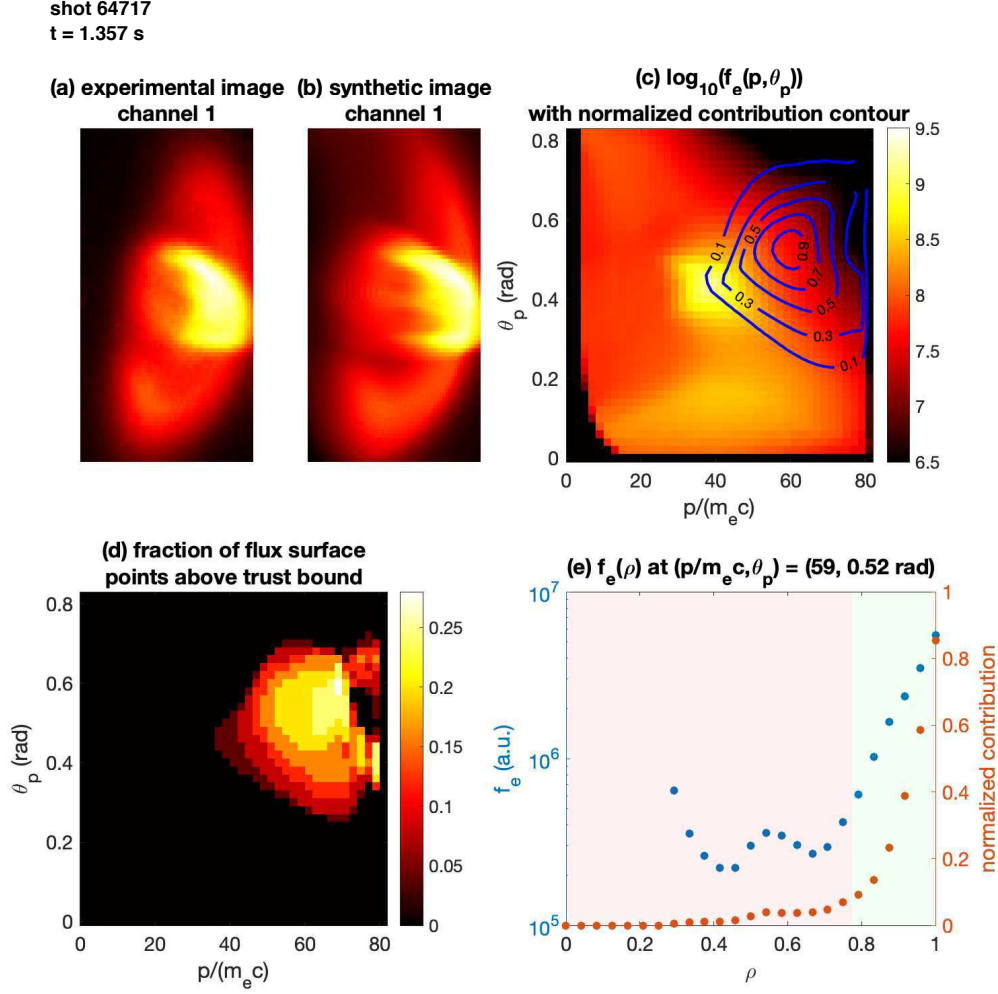


Figure 8. Runaway distribution reconstruction results for TCV shot 64717 at 1.357 s. a) Experimental input image for the SART algorithm. b) Synthetic image after 20 iterations. c) Logarithm of runaway distribution in momentum-space, integrated over all flux surfaces. The contour lines indicate the normalized value of the contribution function GJf_e . d) Number of flux surface points above a normalized contribution threshold of 0.1. e) Logarithm of flux surface distribution at $(p/m_e c, \theta_p) = (59, 0.52 \text{ rad})$. The normalized contribution function at each point is indicated. Only results in the green shaded region are expected to approach the real distribution.

for all camera channels a set of images is generated which complies with the experimental uncertainty. By feeding all images to the SART algorithm one-by-one, N_{image} distribution estimates are obtained. Together, these allow one to construct a mean and standard deviation for the distribution at each point in phase-space. Thus, the propagation of uncertainties in the experimental image to the reconstruction can be quantified.

Figure 9a shows the relation between the mean contribution function GJf_e and the standard deviation in f_e . Better constrained parts of the distribution suffer less from measurement noise. The overall level of uncertainty for GJf_e above 1 percent of the maximum is of the same order as the pixel value uncertainties. The latter are damped by the pixel binning procedure

applied.

Using the same approach the uncertainty introduced by the camera calibration is assessed. Calcam calibrations for MultiCam in TCV typically have a 2 pixel root-mean-square projection error for the calibration points. By applying a horizontal and vertical translation with a value drawn from a distribution with mean 0 and standard deviation of 2 for all three images independently, again a set of N_{image} images are obtained and used for reconstruction. The results are depicted in figure 9b. A similar trend as for the image noise is observed, but the relative uncertainties are roughly two orders of magnitude larger. Above the 10 percent of maximum threshold for the contribution function, relative uncertainties are of the order of 10 to 20 percent.

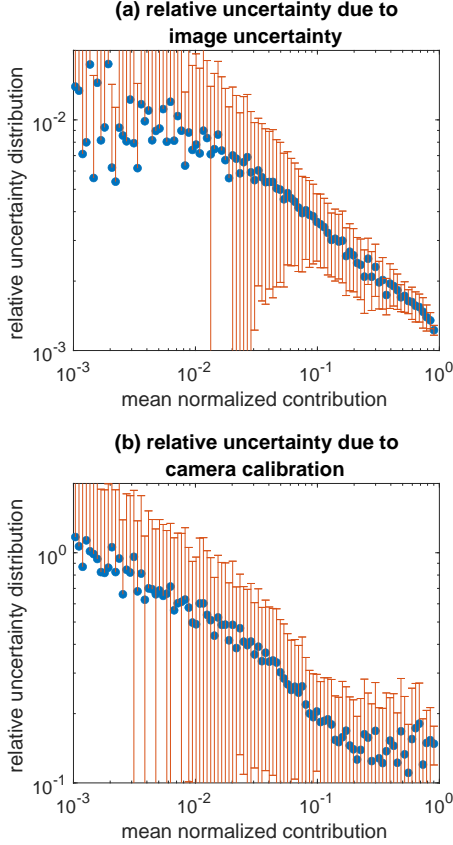


Figure 9. Relative uncertainty in distribution reconstruction as a function of contribution level for shot 64717 at 1.357 s. a) Uncertainty due to noise in input image. b) Uncertainty based on Calcam camera calibration residual pixel error.

It is concluded that errors introduced by reconstruction imperfections, as discussed in chapter 5, are the dominant source of uncertainty. The camera calibration error is however non-negligible. For estimating its magnitude the Monte Carlo uncertainty analysis procedure is time consuming and therefore not suitable for time evolution reconstructions. Taking a few sample points in time, one can however retrieve generic upper bounds for the uncertainty as a function of the phase-space contribution.

6.3. Interpretation of momentum-space distribution

The reconstructed momentum-space distribution is examined in more detail to assess its plausibility. Since $E \gg E_c$, runaways should primarily be generated through the avalanche mechanism, causing their distribution function to decay exponentially with momentum [25]. For momentum-space contribution function values above a 10 percent of the maximum value, this behaviour is indeed found for the flux

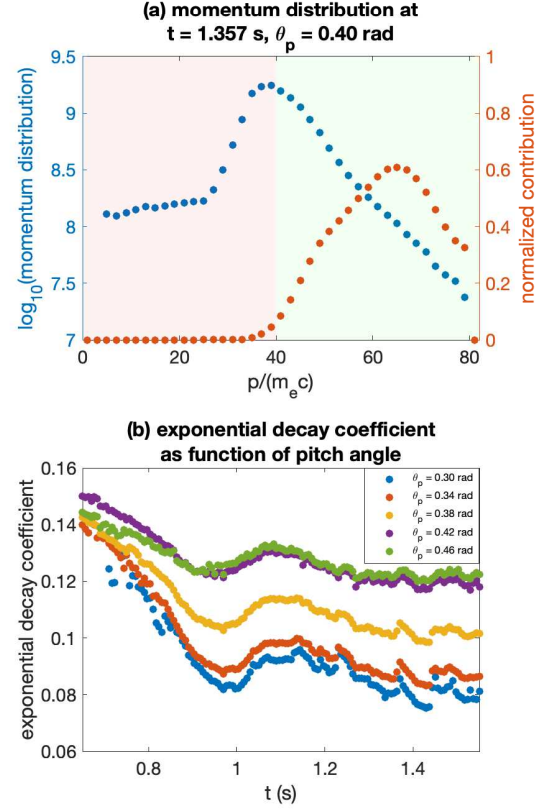


Figure 10. Assessment of shot 64717 momentum runaway profile as obtained using the SART algorithm. a) Logarithm of the flux surface integrated distribution $\sum_{\rho} f_e$ as a function of momentum p , for a pitch angle of 0.40 rad at time $t = 1.357$ s. Decay of f_e appears to be of an exponential nature for sufficiently high contribution values. b) For different pitch angles a linear fit is used to obtain the slope of the exponential decay for the momentum-space points having a contribution value above a fraction of 0.1 of the maximum.

surface integrated reconstructed distribution from figure 8c. Figure 10 shows the distribution as a function of momentum for a pitch angle of 0.40 rad at time $t = 1.357$ s. Above $p/m_e c \sim 40$, $\log_{10}(f_e)$ decays linearly with p . The behaviour is characterized by some decay constant C_p , which from a theoretical point of view is expected to be a function of pitch angle:

$$\sum_{\rho} f_e(\rho, p, \theta_p)|_{\theta_p=\theta_{p,0}} = \text{const} \cdot \exp[-C_p(\theta_{p,0})p], \quad (7)$$

where $\theta_{p,0}$ is the pitch angle under consideration. For various values of $\theta_{p,0}$ the time evolution of the decay constant for $GJf_e > 0.1 \cdot \max(GJf_e)$, as obtained using a least-squares fit, is shown in figure 10b. In general it is observed that the decay constant decreases over time. The equilibrium value of C_p is θ_p dependent, the larger pitch decay constants being found at larger pitch angles. This is consistent with collisional kinetic

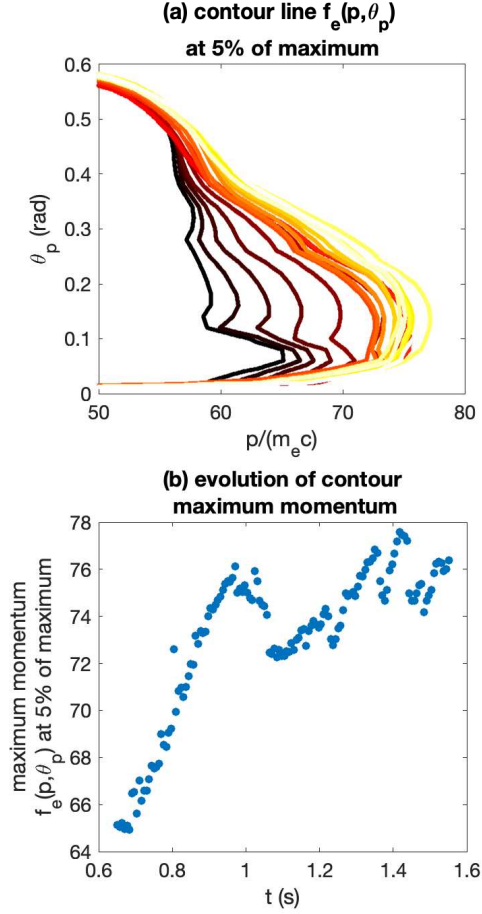


Figure 11. Time evolution of the contour line at 5 percent of the maximum value of the flux surface integrated runaway distribution for shot 64717. a) Time dependence of the contour location. The distribution shifts towards higher momenta until 1.2s. Whereas the front starts out at a nearly uniform value for all pitch angles, the stable momentum location is higher for lower pitch angles. b) Evolution of the maximum momentum value for the contour.

theory and results from the balance between electric field acceleration and pitch angle scattering.

An explanation for the time dependency of C_p is found by examining the time evolution of the flux surface integrated momentum-space profile. The main change in time is the increase in relative occupation of the high momentum part of phase-space. Figure 11a depicts the evolution of the contour line at 5 percent of the maximum of the flux surface integrated momentum profile. The front moves to higher momenta as the runaways are accelerated, as indicated in figure 11b. This momentum increase manifests itself in a decrease in C_p .

The rise in total recorded synchrotron radiation, as shown in figure 3f, is attributed to an increase of the occupation of the high momentum, high pitch angle

part of momentum-space over time. Reconstruction results indicate a population increase over the whole contributing region by a factor of 4.5 or more, which is consistent with the observed integrated intensity trend. Given the rather constant PMTX and MultiCam noise signals, see figure 3, it is not expected that the overall runaway current changes much after 1 s. The main rise in synchrotron signal however occurs between 1 and 1.2s. This discrepancy is likely related to the time required for newly generated runaways to accelerate to the dominantly contributing energies.

The location of the contribution peak at a pitch angle of 0.53 rad is harder to explain. As was pointed out by Hoppe et al. for a similar TCV discharge [14], this value strongly exceeds theoretical expectations. High-frequency kinetic instabilities were proposed as a pitch angle scattering mechanism which could give rise to these anomalously high values of θ_p [26]. For the discussed experiment no diagnostic capable of probing such perturbations starting at frequencies of a several hundred MHz is in place. An alternative pitch angle scattering mechanism is the magnetic field ripple [27], as will be discussed in the next section. At the time of writing no experiments have been performed to address either of these hypotheses.

6.4. Interpretation of flux surface distribution

Until this point in the discussion, the flux surface dependence of the distribution has been disregarded. In the momentum-space region dominating the emission, the reconstruction indicates that the runaway profile peaks at the edge, as shown in figure 8e. No statements are made on the radial distribution at low energies and pitch angles, as these are poorly constrained. The same is true for the distribution shape in the plasma centre. GJf_e contribution values indicate that conclusions about the runaway density profile can only be drawn for the machine minor radii $\rho > 0.4$.

The rather surprising increase of the radial density profile between $\rho = 0.4$ and $\rho = 1$ could find its origin in the same mechanism as the anomalously high observed pitch angles. Possibly, the mechanism scattering the REs perpendicular to the field lines significantly gains in strength towards the edge of the plasma.

A pitch angle scattering mechanism which lines up with this hypothesis is the magnetic field ripple. Resonant interaction can occur between runaways gyrating at their relativistically downshifted electron cyclotron frequency and the modulations in the toroidal field caused by the finite amount of toroidal field coils [27]. The value of γ for which the resonance occurs is roughly

$$\gamma_{\text{ripple}} = \frac{eBR}{m_e c n_{\text{res}} N_{\text{coils}}}, \quad (8)$$

where n_{res} is the resonant mode number and N_{coils} is the number of toroidal field coils. For shot 64717, the $n_{\text{res}} = 1 - 3$ resonances are expected to occur near normalized momenta of 46, 23 and 15 respectively. The interaction strength decreases with mode number, and increases moving closer towards the coils at larger minor radius. Runaway-field ripple interaction is not expected to yield an energy barrier given the large prevailing electric fields [28]. However, runaways accelerating through these resonances are expected to undergo significant pitch angle scattering. Because of the increasing interaction strength moving towards the edge of the plasma, the momentum-space region dominating the synchrotron emission could thus realistically have the a shape depicted in figure 8e. Note that the part of momentum-space contributing to the image has normalized momentum starting at roughly 40, which could indicate interaction of the runaways with the $n_{\text{res}} = 1$ resonance. Testing of the ripple hypothesis would be aided by experiments in which the magnetic field strength is varied.

As pointed out by Hoppe et al [14], the high pitch angles could also result from an interaction with high frequency plasma instabilities. Strong experimental evidence of such events backed up by kinetic simulations has been reported for DIII-D [26, 29]. For the present experiments, this mechanism does not directly explain the increase in population towards the edge of the plasma at high pitch angles and momenta. A mechanism which could account for this profile is the build up of a runaway shell at the edge of the plasma during startup. As the loop voltage is initially peaked at the edge a local runaway shell could form. Due to its high conductivity it could act as a partial barrier for the electric field, sustaining an edge peaked profile for the runaways while allowing Ohmic current drive in the core.

7. Summary and conclusions

This work elaborates on recent advances in multispectral camera analysis of runaway synchrotron radiation. 2D synchrotron profiles obtained through absolutely calibrated cameras with the same field-of-view but different central filter wavelength, provide both spatial and spectral resolution. It is found that:

The spatial and spectral resolution of runaway synchrotron patterns offered by multispectral camera systems provide a complementary widening of the probed region of momentum-space.

Strengthened by the improved level of constraint on the runaway distribution, the tomographic SART method is used for the first time to provide a distribution reconstruction with no constraint on the

momentum-space profile. The outlined approach relies on the synthetic diagnostic SOFT to provide a response function linking an arbitrary distribution in guiding-center coordinates to pixel intensities on a specified detector. Using a test distribution to generate a set of corresponding images through a response function, the performance of the approach is assessed. The three main conclusions are:

- i) Provided an absolutely calibrated camera system the SART algorithm can be used to locally reconstruct the runaway phase-space distribution with an accuracy better than a factor of 2. No constraints on the shape of the momentum- or spatial-profile are required, and sharp gradients in the distribution can be dealt with.
- ii) The contribution of each phase-space element to reconstructed images is a robust measure for the level of trust to be placed in local reconstruction accuracy.
- iii) Increasing the number of spectral channels used as constraints for the reconstruction improves the accuracy of the distribution reconstruction.

Next, the algorithm is put to the test using multispectral synchrotron data from the MultiCam system in TCV tokamak. The observed patterns, with highly distinctive geometric features, are accurately reconstructed. It is found that the runaways dominating the emission have $p/m_e c$ in excess of 40 and pitch angles above 0.30 rad. The contribution peak is found at $(p/m_e c, \theta_p) = (60, 0.53 \text{ rad})$, consistent with earlier estimates using a super-particle approach [14]. At these high momenta and pitch angles the reconstructed profile increases above a normalized radius of $\rho > 0.4$ towards the edge. Note that this does not imply that the overall runaway current exhibits a hollow profile.

The physical plausibility of the TCV runaway reconstruction is addressed. It is found that:

Runaway distribution reconstructions from TCV multispectral synchrotron data show an exponential decay with increasing particle momentum, as is expected for an avalanche-dominated distribution in equilibrium. Time sequence reconstructions show a relaxation of the momentum distribution with a pitch angle dependency consistent with collisional kinetic theory.

Additional experiments are needed to understand the pitch angle and spatial distribution:

Pitch angles in the phase-space region contributing most to the synchrotron image are anomalously high. a toroidal field ripple is proposed as a candidate for pitch angle scattering.

This picture is consistent with an increase in occupation of these high pitch angles moving from the core of the plasma towards the edge. An alternative explanation is found in high frequency plasma instabilities in combination with the formation of a runaway shell at the edge during startup, limiting electric field penetration towards the core of the plasma.

Further experiments are needed to address both hypotheses. These efforts will be strengthened by the enhanced runaway distribution details which the advances in multispectral imaging systems and the use of the SART method enable.

Acknowledgments

DIFFER is part of the institutes organisation of NWO. This work has been carried out within the framework of the EUROfusion Consortium and has received funding from the Euratom research and training programme 2014-2018 and 2019-2020 under grant agreement No 633053. The views and opinions expressed herein do not necessarily reflect those of the European Commission.

References

- [1] E.M. Hollmann, P.B. Aleynikov, T. Fülöp, D.A. Humphreys, V.A. Izzo, M. Lehnen, V.E. Lukash, G. Papp, G. Pautasso, F. Saint-Laurent, and J.A. Snipes. Status of research toward the ITER disruption mitigation system. *Physics of Plasmas*, 22(2):021802, 2015. doi:10.1063/1.4901251.
- [2] M. Lehnen et al. Disruptions in ITER and strategies for their control and mitigation. *Journal of Nuclear Materials*, 463:39 – 48, 2015. doi:10.1016/j.jnucmat.2014.10.075.
- [3] B.N. Breizman, P. Aleynikov, E.M. Hollmann, and M. Lehnen. Physics of runaway electrons in tokamaks. *Nuclear Fusion*, 59(8):083001, 2019. doi:10.1088/1741-4326/ab1822.
- [4] M. Hoppe, O. Embréus, C. Paz-Soldan, R.A. Moyer, and T. Fülöp. Interpretation of runaway electron synchrotron and bremsstrahlung images. *Nuclear Fusion*, 58(8):082001, 2018. doi:10.1088/1741-4326/aaae15.
- [5] K.H. Finken, J.G. Watkins, D. Rusbüldt, W.J. Corbett, K.H. Dippel, D.M. Goebel, and R.A. Moyer. Observation of infrared synchrotron radiation from tokamak runaway electrons in TEXTOR. *Nuclear Fusion*, 30(5):859–870, 1990. doi:10.1088/0029-5515/30/5/005.
- [6] R. Jaspers, N.J. Lopes Cardozo, K.H. Finken, B.C. Schokker, G. Mank, G. Fuchs, and F.C. Schüller. Islands of runaway electrons in the TEXTOR tokamak and relation to transport in a stochastic field. *Physical Review Letters*, 72:4093–4096, 1994. doi:10.1103/PhysRevLett.72.4093.
- [7] R.A. Tinguely, R.S. Granetz, M. Hoppe, and O. Embréus. Spatiotemporal evolution of runaway electrons from synchrotron images in Alcator C-Mod. *Plasma Physics and Controlled Fusion*, 60(12):124001, 2018. doi:10.1088/1361-6587/aae6ba.
- [8] R.A. Tinguely, R.S. Granetz, M. Hoppe, and O. Embréus. Measurements of runaway electron synchrotron spectra at high magnetic fields in Alcator C-Mod. *Nuclear Fusion*, 58(7):076019, 2018. doi:10.1088/1741-4326/aac444.
- [9] A. Stahl, M. Landreman, G. Papp, E. Hollmann, and T. Fülöp. Synchrotron radiation from a runaway electron distribution in tokamaks. *Physics of Plasmas*, 20(9):093302, 2013. doi:10.1063/1.4821823.
- [10] Y. Shi, J. Fu, J. Li, Y. Yang, F. Wang, Y. Li, W. Zhang, B. Wan, and Z. Chen. Observation of runaway electron beams by visible color camera in the Experimental Advanced Superconducting Tokamak. *Review of Scientific Instruments*, 81(3):033506, 2010. doi:10.1063/1.3340909.
- [11] J.H. Yu, E.M. Hollmann, N. Commaux, N.W. Eidietis, D.A. Humphreys, A.N. James, T.C. Jernigan, and R.A. Moyer. Visible imaging and spectroscopy of disruption runaway electrons in DIII-D. *Physics of Plasmas*, 20(4):042113, 2013. doi:10.1063/1.4801738.
- [12] R.J. Zhou, I.M. Pankratov, L.Q. Hu, M. Xu, and J.H. Yang. Synchrotron radiation spectra and synchrotron radiation spot shape of runaway electrons in Experimental Advanced Superconducting Tokamak. *Physics of Plasmas*, 21(6):063302, 2014. doi:10.1063/1.4881469.
- [13] M. Hoppe, O. Embréus, R.A. Tinguely, R.S. Granetz, A. Stahl, and T. Fülöp. SOFT: a synthetic synchrotron diagnostic for runaway electrons. *Nuclear Fusion*, 58(2):026032, 2018. doi:10.1088/1741-4326/aa9abb.
- [14] M. Hoppe, G. Papp, T.A. Wijkamp, J. Decker, B.P. Duval, O. Embréus, T. Fülöp, U. A. Sheikh, TCV Team, and EUROfusion MST1 Team. Runaway electron synchrotron radiation in a vertically translated plasma. *Nuclear Fusion*, 60(9):094002, 2020. doi:10.1088/1741-4326/aba371.
- [15] M. Hoppe, L. Hesslow, O. Embréus, L. Unnerfelt, G. Papp, I. Pusztai, T. Fülöp, O. Lexell, T. Lunt, E. Macusova, P.J. McCarthy, G. Pautasso, G.I. Pokol, G. Por, P. Svensson, the ASDEX Upgrade team, and the EUROfusion MST1 team. Spatiotemporal analysis of the runaway distribution function from synchrotron images in an ASDEX Upgrade disruption. *Under consideration in Journal of Plasma Physics*, 2020. URL: <https://arxiv.org/abs/2005.14593>.
- [16] A. Perek, W.A.J. Vijvers, Y. Andrebe, I.G.J. Classen, B.P. Duval, C. Galperti, J.R. Harrison, B.L. Linehan, T. Ravensbergen, K. Verhaegh, and M.R. de Baar. MANTIS: A real-time quantitative multispectral imaging system for fusion plasmas. *Review of Scientific Instruments*, 90(12):123514, 2019. doi:10.1063/1.5115569.
- [17] A. Perek, B.L. Linehan, M. Wensing, K. Verhaegh, I.G.J. Classen, B.P. Duval, O. Février, H. Reimerdes, C. Theiler, T. A. Wijkamp, M.R. de Baar, the EUROfusion MST1 team, and the TCV team. Measurement of the 2D emission profiles of the bulk and impurity ions in the TCV divertor. *Submitted to Journal of Nuclear Materials and Energy*, 2020. doi:10.13140/RG.2.2.21477.42720.
- [18] S. Silburn, J. Harrison, M. Smithies, A. Wynn, T. Farley, and J. Cavalier. Calcam (version 2.5.0). <https://github.com/euratom-software/calcam/tree/v2.2.0>, 2020. doi:10.5281/zenodo.3956834.
- [19] J. Hawke, Y. Andrebe, R. Bertizzolo, P. Blanchard, R. Chavan, J. Decker, B.P. Duval, P. Lavanchy, X. Llobet, B. Marlétaz, P. Marmillod, G. Pochon, and M. Toussaint. Improving spatial and spectral resolution of TCV thomson scattering. *Journal of Instrumentation*, 12(12):C12005–C12005, 2017. doi:10.1088/1748-0221/12/12/c12005.

- [20] J.W. Connor and R.J. Hastie. Relativistic limitations on runaway electrons. *Nuclear Fusion*, 15(3):415–424, 1975. doi:10.1088/0029-5515/15/3/007.
- [21] J.M. Moret, B.P. Duval, H.B. Le, S. Coda, F. Felici, and H. Reimerdes. Tokamak equilibrium reconstruction code LIUQE and its real time implementation. *Fusion Engineering and Design*, 91:1 – 15, 2015. doi:10.1016/j.fusengdes.2014.09.019.
- [22] X. Guan, H. Qin, and N.J. Fisch. Phase-space dynamics of runaway electrons in tokamaks. *Physics of Plasmas*, 17(9):092502, 2010. doi:10.1063/1.3476268.
- [23] A.H. Andersen and A.C. Kak. Simultaneous algebraic reconstruction technique (SART): A superior implementation of the art algorithm. *Ultrasonic Imaging*, 6(1):81 – 94, 1984. doi:10.1016/0161-7346(84)90008-7.
- [24] M. Carr, A. Meakins, M. Bernert, P. David, C. Giroud, J. Harrison, S. Henderson, B. Lipschultz, and F. Reimold. Description of complex viewing geometries of fusion tomography diagnostics by ray-tracing. *Review of Scientific Instruments*, 89(8):083506, 2018. doi:10.1063/1.5031087.
- [25] T. Fülöp, G. Pokol, P. Helander, and M. Lisak. Destabilization of magnetosonic-whistler waves by a relativistic runaway beam. *Physics of Plasmas*, 13(6):062506, 2006. doi:10.1063/1.2208327.
- [26] C. Liu, E. Hirvijoki, G. Fu, D.P. Brennan, A. Bhattacharjee, and C. Paz-Soldan. Role of kinetic instability in runaway-electron avalanches and elevated critical electric fields. *Physical Review Letters*, 120:265001, 2018. doi:10.1103/PhysRevLett.120.265001.
- [27] A.J. Russo. Effect of ripple on runaway electrons in tokamaks. *Nuclear Fusion*, 31(1):117–126, 1991. doi:10.1088/0029-5515/31/1/011.
- [28] J.R. Martín-Solís, B. Esposito, R. Sánchez, and J.D. Alvarez. Energy limits on runaway electrons in tokamak plasmas. *Physics of Plasmas*, 6(1):238–252, 1999. doi:10.1063/1.873276.
- [29] Paz-Soldan C., N.W. Eidietis, E.M. Hollmann, P. Aleynikov, L. Carbajal, W.W. Heidbrink, M. Hoppe, C. Liu, A. Lvovskiy, D. Shiraki, D. Spong, D.P. Brennan, C.M. Cooper, D. del Castillo-Negrete, X. Du, O. Embreus, T. Fulop, J. Herfindal, R. Moyer, P. Parks, and K.E. Thome. Recent DIII-D advances in runaway electron measurement and model validation. *Nuclear Fusion*, 59(6):066025, 2019. doi:10.1088/1741-4326/ab1769.